nuclear fusion
IAEA

PAPER • OPEN ACCESS

Inference of main ion particle transport coefficients with experimentally constrained neutral ionization during edge localized mode recovery on DIII-D

To cite this article: A.M. Rosenthal *et al* 2023 *Nucl. Fusion* **63** 042002

View the article online for updates and enhancements.

You may also like

- Performance Simulation of Tubular Segmented-in-Series SOFC Using Simplified Equivalent Circuit
Shun Yoshida, Tadashi Tanaka and Yoshitaka Inui
- *(Invited)* Potential of Double Network Gel as a Tribological Material Realizing Low Friction in Water
Koki Kanda and Koshi Adachi
- Analysis of the Effect of Surface Diffusion on Effective Diffusivity of Oxygen in Catalyst Layer By Direct Simulation Monte Carlo
Tomoki Hori, Takuya Mabuchi, Ikuya Kinefuchi et al.

This content was downloaded from IP address 3.147.104.120 on 25/04/2024 at 05:14

OPEN ACCESS
IOP Publishing | International Atomic Energy Agency
Nuclear Fusion
Nucl. Fusion **63** (2023) 042002 (11pp)
https://doi.org/10.1088/1741-4326/acb95a

Inference of main ion particle transport coefficients with experimentally constrained neutral ionization during edge localized mode recovery on DIII-D

A.M. Rosenthal[1,*], J.W. Hughes[1], F.M. Laggner[2], T. Odstrčil[3], A. Bortolon[4], T.M. Wilks[1] and F. Sciortino[5]

[1] Plasma Science and Fusion Center, Massachusetts Institute of Technology, 175 Albany Street, Cambridge, MA 02139, United States of America
[2] Department of Nuclear Engineering, North Carolina State University, Raleigh, NC 27607, United States of America
[3] General Atomics, San Diego, CA 92186-5608, United States of America
[4] Princeton Plasma Physics Laboratory, Princeton, NJ 08543, United States of America
[5] Max-Planck-Institute of Plasma Physics, Boltzmannstraße 2, Garching, Bayern 85748, Germany

E-mail: aaronmr@mit.edu

Received 18 November 2022, revised 31 January 2023
Accepted for publication 6 February 2023
Published 1 March 2023

Abstract

The plasma and neutral density dynamics after an edge localized mode are investigated and utilized to infer the plasma transport coefficients for the density pedestal. The Lyman-Alpha Measurement Apparatus (LLAMA) diagnostic provides sub-millisecond profile measurements of the ionization and neutral density and shows significant poloidal asymmetries in both. Exploiting the absolute calibration of the LLAMA diagnostic allows quantitative comparison to the electron and main ion density profiles determined by charge-exchange recombination, Thomson scattering and interferometry. Separation of diffusion and convection contributions to the density pedestal transport are investigated through flux gradient methods and time-dependent forward modeling with Bayesian inference by adaptation of the Aurora transport code and IMPRAD framework to main ion particle transport. Both methods suggest time-dependent transport coefficients and are consistent with an inward particle pinch on the order of 1 m s^{-1} and diffusion coefficient of 0.05 m^2 s^{-1} in the steep density gradient region of the pedestal. While it is possible to recreate the experimentally observed phenomena with no pinch in the pedestal, low diffusion in the core and high outward convection in the near scrape-off layer are required without an inward pedestal pinch.

Keywords: VUV spectroscopy, fusion energy, tokamaks, pedestal transport, plasma confinement

(Some figures may appear in colour only in the online journal)

* Author to whom any correspondence should be addressed.

Original Content from this work may be used under the terms of the Creative Commons Attribution 4.0 licence. Any further distribution of this work must maintain attribution to the author(s) and the title of the work, journal citation and DOI.

1. Introduction

Achieving high fusion power in tokamaks utilizing high confinement mode (H-mode) requires an improved understanding of the edge region in current devices and prediction of future burning plasma devices. The edge pedestal is a region, a few centimeters wide, near the edge of a tokamak plasma where steep gradients form due to a transport barrier correlated with high energy confinement. Since the fusion power density, P, generated by tokamaks is related to the density n as $P \sim n^2$, and core transport is frequently considered stiff, the density pedestal dramatically improves the global plasma performance [1]. Despite the importance of the density pedestal to global performance, there is a relative lack of understanding of the fundamental processes that guide and limit the density pedestal's formation in current devices, leading to significant uncertainties in projections for future devices.

Understanding the edge density pedestal is challenging due to the small spatial scales, complex plasma transport properties, and presence of ionizing neutral particles. In particular, the role and scaling of the neutral particle source in the density pedestal have yet to be determined. Furthermore, neutral particles directly enter into edge 2D modeling codes and physical models of the edge [2–7]. The neutral particle source is difficult to measure experimentally. For example, when using Balmer-alpha, molecular radiation contributes to line brightness and reflections are non-negligible. While measuring Lyman-alpha (Ly-α) radiation to determine the particle source is challenging due to optic limitations in the vacuum ultra-violet and the need for components to be in vacuum. Recently, DIII-D installed the Lyman-Alpha Measurement Apparatus (LLAMA) diagnostic to provide radially and temporally resolved measurements of the hydrogenic Ly-α brightness used to determine the neutral particle and ionization source in the pedestal region at two poloidal locations without advanced modeling [8]. The LLAMA diagnostic is absolutely calibrated, providing a quantitative measurement of the hydrogenic neutral density and ionization rate which can be directly compared to the main ion density [9]. Thus, LLAMA provides a unique opportunity at DIII-D for density pedestal transport studies.

In present-day tokamaks, studies of the density pedestal have focused on the relative role of fueling versus plasma transport in forming the density pedestal [10]. The diffusive-convective ansatz, $\Gamma = -D\nabla n + vn$ provides an experimentally testable model linking the evolution of the density profile, n, to the particle fluxes, Γ, through the transport coefficients diffusion (D) and convection (v). The particle flux is in turn linked to the particle source S by the continuity equation $\frac{\partial n}{\partial t} = -\nabla \cdot \Gamma + S$. While main ion transport studies of the D and v coefficients were carried out in the core of the plasma, it is complicated at the edge of the plasma where the source is non-negligible [11–16]. Of particular interest is whether an inward particle pinch exists in the pedestal, which would allow fueling and possibly the formation of a steep density gradient even when hydrogenic ionization moves into the Scrape-Off Layer (SOL), as expected in future devices.

In the pedestal, multiple methods have been employed to gain insight into the transport coefficients by examining both steady state and dynamic events. Steady-state methods are limited to modeling fluxes as purely diffusive or convective. Or, steady-state analysis assumes transport is constant across discharges and time windows with varying density gradients and absolute values. Previous steady-state studies reported transport coefficients with large uncertainties or as a purely diffusive process [10, 17, 18]. Examination of dynamic events offers more precise disentangling of the relative contributions of D and v by examining dynamics of the density gradient and absolute values as they evolve within a single discharge. However, time-dependent analysis frequently requires interpretive modeling, high temporal-resolution diagnostics and more advanced analysis techniques. Previous studies of dynamic events have utilized gas puff modulation, L–H transitions, and the density rebuild after an Edge Localized Mode (ELM) to investigate the transport processes [19–23]. However, previous dynamic studies have relied on modeling the edge ionization source profile utilizing 1.5 D codes which are frequently not experimentally validated and do not contain full time dependence. Here, the absolutely calibrated time-dependent edge ionization source profiles from the LLAMA diagnostic are utilized to constrain the edge particle source experimentally.

The density rebuild after an ELM is utilized to investigate the relative contributions of D and v in the pedestal with experimentally constrained edge deuterium source measurements. Section 2 highlights the discharge and diagnostics details. Section 3 details the analysis procedures for providing ionization and neutral density measurements for hydrogenic isotopes using the LLAMA diagnostic. The qualitative evolution of the electron density, neutral density, and ionization dynamics are highlighted in section 4. Finally, section 5 introduces methods to calculate D and v independently from dynamic events using both an analytic approach and more advanced forward modeling. Forward modeling, with Aurora coupled to Bayesian inference through IMPRAD is utilized to quantitatively infer time-dependent transport coefficients. The analytic and forward modeling approaches are consistent with an inward main ion convection (pinch) in the steep density gradient region.

2. Discharge and diagnostic details

All data discussed in this paper come from a lower single null (LSN) deuterium discharge in the ITER similar shape. The shape was selected due to good edge diagnostic coverage from the LLAMA, Thomson Scattering (TS) and Charge-exchange Recombination Spectroscopy (CER) systems [8, 24, 25]. The plasma shape and diagnostic coverage can be seen in figure 1(a). The plasma current, line average density, and toroidal magnetic field are 1.5 MA, 8×10^{19} m^{-3} and 2 T respectively. The magnetic field is oriented in the 'favorable' drift direction for a lower power threshold for the transition to H-mode, with the $B \times \nabla B$ drift toward the active X-point.

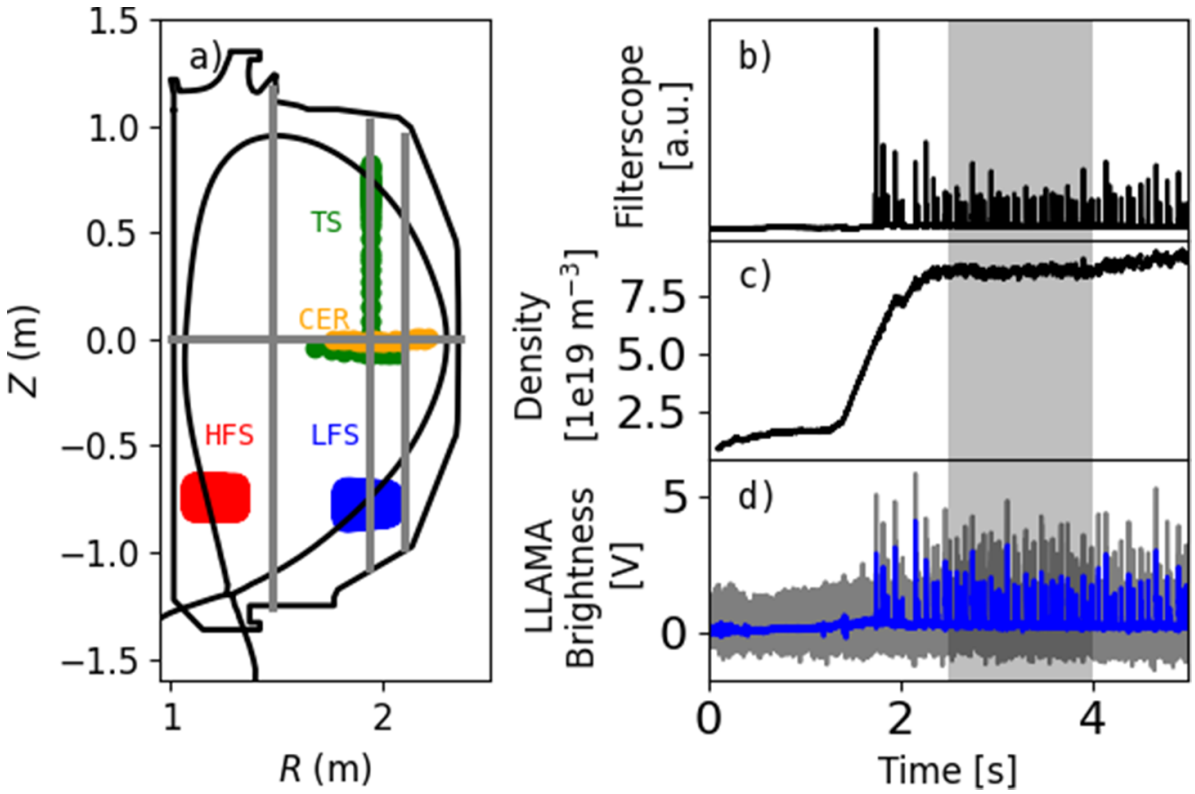

Figure 1. Overview of studied discharge, 180907 (*a*) last closed flux surface (LCFS) (black) for the lower single null (LSN) ITER similar shape. The projection of the LLAMA views onto their tangency radius are shown for the high field side (HFS) (red) and low field side (LFS) (blue). Also shown are the Thomson Scattering (TS) measurement locations (green), CO 2 Interferometer chords (grey), and tangential Charge-exchange Recombination Spectroscopy (CER) views (orange). (*b*) Time trace of photodiode channel used to identify ELMs. (*c*) Line average density (*d*) raw (black) and filtered (blue) LLAMA signal for a single low field side (LFS) channel. The time period studied is highlighted in grey.

Once the plasma transitions into H-mode, ELMs occur, with each resulting in a five to ten percent loss in line average density. Analysis is restricted to the stationary ELMy H-mode period from 2500 ms to 4000 ms, highlighted in grey in figures 1(*b*)–(*d*). During this period, the shape, neutral beam injection (NBI) heating power and strike point are all held constant. The time between ELM's is typically 40 ms with some lasting up to 80 ms. To improve temporal coverage by all diagnostics, the first 40 ms of all ELM cycles are included in the analysis.

The TS system and CO_2 interferometer measurements are utilized to determine the electron density and temperature profiles through simultaneous fitting in radial and temporal dimensions. The two dimensional fitting algorithm calculates a smooth surface in time and radial space without constraints on the shape of the profile. The algorithm requires specification of the time and radial scale of the smoothed fit, similar to the 2D Gaussian regression detailed in [26]. For electron density, TS measurements are scaled to match the line-averaged interferometer measurements [24, 27]. The main ion density is inferred from the electron density fits using a two dimensional fitting algorithm and CER measurements of the density of the fully stripped carbon ions [25]. Due to the carbon walls of DIII-D, carbon is the main impurity in the plasma. Therefore, the dilution of the main ion is calculated assuming fully stripped carbon is the sole impurity. Furthermore, since the density of non-fully stripped carbon is poorly constrained in the pedestal, it is assumed that the dilution from carbon is flat throughout the plasma. These assumptions result in a radially uniform scaling of the electron density by 0.7 to calculate the main ion density.

3. Reconstruction of neutral density and ionization rate profiles from LLAMA

Providing local measurements of the ionization rate and neutral density from experimental measurements of Ly-α brightness from LLAMA is achieved through four steps:

(a) Ly-α brightness is processed by noise filtering and offset subtraction.
(b) An inversion is then performed using a 1D tomographic inversion [28].
(c) Electron density and electron temperature are assumed to be flux surface functions and mapped to a common radial grid with the emissivity measurements.
(d) Finally, ADAS rate coefficients are evaluated to determine the ionization rate and neutral density [29].

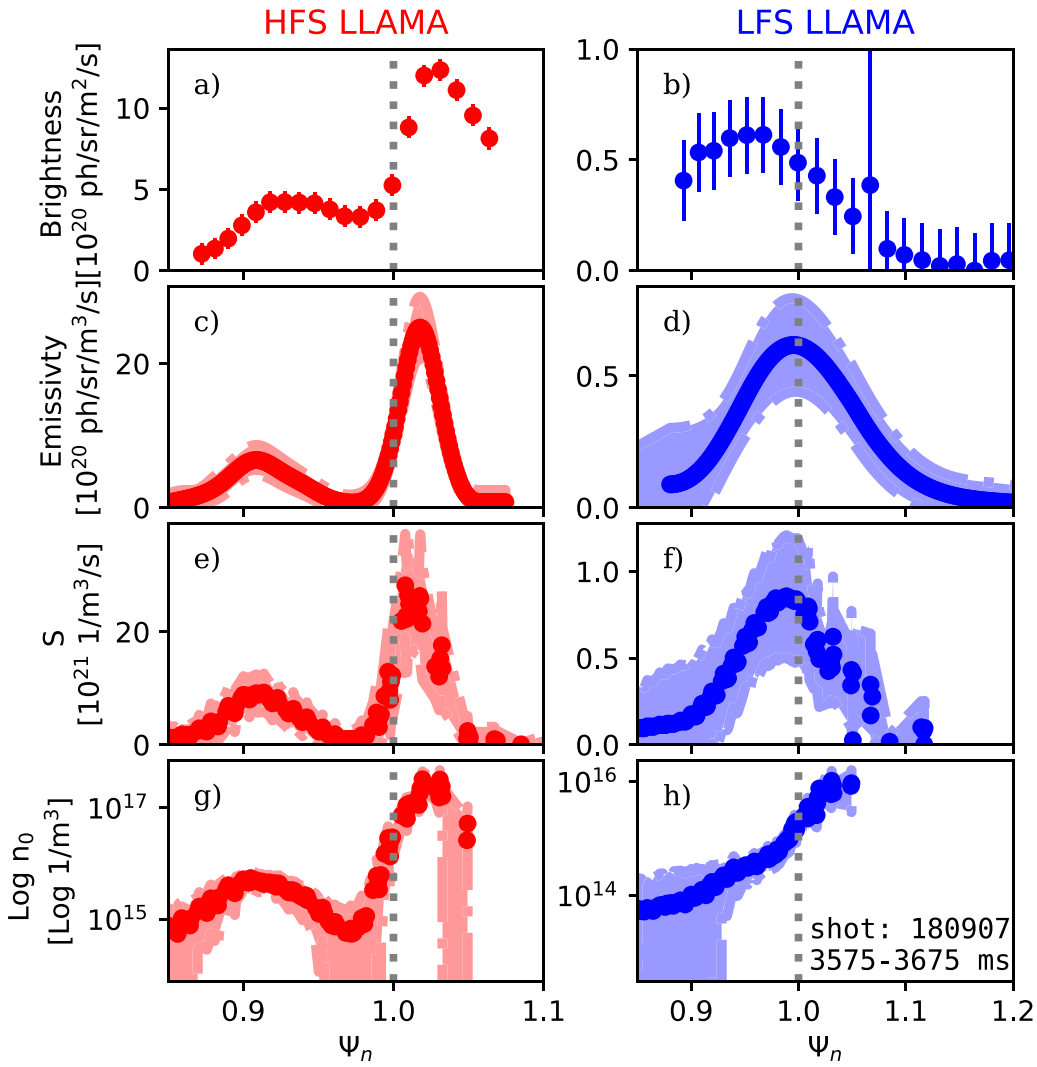

Figure 2. Time averaged ELM synchronized profiles, including the last 30% of the ELM cycle, of the Ly-α brightness (*a*) and (*b*) profiles from the high field side (HFS) (red) and low field side (LFS) (blue) LLAMA system. (*c*) and (*d*) The local emissivity is inferred through a 1D tomographic code. The deuterium ionization rate (*e*) and (*f*) and neutral density (*g*) and (*h*) are then calculated using electron density and electron temperature measurements to evaluate ADAS rate coefficients.

As, an example of the data analysis procedure, a steady state, ELM synchronized, window is analyzed, shown in figure 2. The steady state behavior is taken from the last 30% of the ELM cycle for the time window from 3575 to 3675 ms and the brightness is averaged before the 1D tomographic inversion is performed.

In the first step, measured brightness by LLAMA, which is the emissivity integrated along the line of sight, is processed through an advanced filtering algorithm [30]. The algorithm removes electronic high frequency noise induced in the LLAMA system from high voltage power supplies which are used to drive currents in the magnetic coils that control the tokamak plasma. The algorithm identifies linear, time-invariant, multi-input single output systems and results in a 10–20 dB reduction in noise in the 1–10 kHz range. The signals are then binned in time. DC offsets for each channel are individually removed by subtracting the mean voltage 500 ms before the plasma breakdown. Finally, a mean of the three outermost channels is subtracted from all channels in both systems to remove remaining residual pickup noise, which assumes that no Ly-α signal is observed in those outermost channels. Error bars in the brightness are estimated from differences in variation of the brightness from neighboring LLAMA channels as well as from the outermost subtracted channels. Processed brightness profiles can be seen in panels (*a*) and (*b*) of figure 2.

Emissivity is calculated by the inversion of the processed line average brightness. The emissivity, shown in figures 2(*c*) and (*d*), is calculated by a one-dimensional tomographic inversion [28] which exploits the toroidal views of LLAMA. Each channel's radial spot size and expansion along its line of sight is incorporated in the inversion process. The low field side (LFS) and high field side (HFS) views are inverted independently, with the LFS's contribution to the HFS's line integrated brightness removed. The HFS views do not pass through the neutral beam system, and the relative path lengths,

compared to the tangency radius, are small. Therefore, it is assumed that a negligible amount of Ly-α radiation from the core, including Bremhsstrahlung radiation, contributes to the observed HFS brightness. Error bars in the reported emissivity profile come from the absolute calibration factor error and uncertainty from the inversion [9]. The inversion uncertainty is estimated by back projections of inversion profiles which match the experimental brightness measurements.

Neutral deuterium ionization rates and densities, shown in figures 2(*e*)–(*h*), are inferred from the local emissivity, electron density (n_e), electron temperature (T_e) and ion density (n_i) using ADAS rate coefficients. Rate coefficients from a collisional radiative model depend on line electron density (n_e) and electron temperature (T_e) [29]. ADAS ADF15 and ADF11 photon emissivity coefficient (PEC) for excitation ($\mathrm{PEC}^{\mathrm{exc}}_{2\rightarrow1}$), PEC for recombination ($\mathrm{PEC}^{\mathrm{rec}}_{2\rightarrow1}$), and effective ionisation coefficient (SCD), from files `pec12#h_pju#h0.dat` and `scd12h.dat`, are utilized to relate the observed emissivity to the ionization rate (S) and the neutral density (n_0). The following equations for S and n_0 are utilized:

$$S = 4\pi E_{\mathrm{ly}-\alpha}\frac{\mathrm{SCD}_{2\rightarrow1}(T_e,n_e)}{\mathrm{PEC}^{\mathrm{exc}}_{2\rightarrow1}(T_e,n_e)} \tag{1}$$

$$n_0 = \frac{4\pi E_{\mathrm{ly}-\alpha} - \mathrm{PEC}^{\mathrm{rec}}_{2\rightarrow1}(T_e,n_e)n_i n_e}{\mathrm{PEC}^{\mathrm{exc}}_{2\rightarrow1}(T_e,n_e)n_e} \tag{2}$$

where emissivity is in units photons $\mathrm{sr}^{-1}\,\mathrm{m}^{-3}\,\mathrm{s}^{-1}$. The $\mathrm{PEC}^{\mathrm{rec}}_{2\rightarrow1}$ is typically over six orders of magnitude smaller than the excitation coefficient near the pedestal and can therefore be ignored. It is worth noting that for temperatures above 100 eV, typical inside the last closed flux surface (LCFS), the ratio of SCD to $\mathrm{PEC}^{\mathrm{exc}}_{2\rightarrow1}$ is insensitive to changes in T_e and n_e making S a particularly robust inferred quantity. Uncertainties in inferred quantities are derived from measurement uncertainties and mapping of the LLAMA channels onto the common radial grid. EFIT mapping uncertainty is not included since the LLAMA full-width half maximum is approximately 2 cm [8], dominating the spatial uncertainty from EFIT mappings which are approximately 2 mm at the separatrix outer mid-plane [31].

The detailed procedure for calculating hydrogenic ionization rates and neutral density using Ly-α measurements highlights how main ion source measurements can be determined from closed form equations. Furthermore, while the example data analysis focused on a steady state scenario by examining ELM synchronized time windows, the procedure is general and can be made time dependent to exploit the LLAMA temporal resolution.

4. Ionization and neutral density profile evolution through the ELM cycle

ELMs are of interest in tokamaks for a variety of reasons: they limit the growth of the density pedestal, pose a threat to plasma facing components, and help flush impurities from the core, to name a few. Theoretical efforts have made strides in explaining the onset of ELMs using peeling–balloning models [32]. However, understanding of the recovery of the post-ELM electron density pedestal is limited. Studies have focused on the qualitative evolution of the electron density gradient, the behavior of edge fluctuations through the elm cycle and the role of the plasma current on the time-scale of ELM-evolution [33–37]. A persistent question has been the role of neutral particles and the source ionization in the density rebuild [3]. Recent experimental work has successfully shown the evolution of the ionization rate and neutral density profiles in an ELM cycle for the LFS utilizing neutral particle analyzers and FIDASIM on the ASDEX tokamak [38]. LLAMA allows experimental measurement of neutral dynamics and ionization evolution in two locations on DIII-D, further characterizing the poloidally varying nature of the problem.

Figure 3 highlights the observed evolution of the electron density, deuterium ionization and deuterium neutral density from both LLAMA views throughout an ELM cycle. Data are taken from about 30 ELM cycles which were identified from a Balmer-alpha (B-α) filterscope, shown in figure 1(*b*). Ly-α brightness data from all ELM cycles is combined by recasting the time axis as absolute time from the previous ELM. The brightness data are filtered and then averaged in a 0.5 ms window and inverted as described in section 3. Mapping of the emissivity onto the common normalized poloidal flux (Ψ_N) grid with the density and temperature measurements is done by calculating an average mapping from the radial coordinates to the Ψ_N grid using EFITs from all times within the analysis window. Error in the mapping is estimated from the variation in the EFITs and the LLAMA channel size. For the electron density measurements, the time axis is recast in the same manner as the Ly-α measurements before being fitted utilizing the two-dimensional gaussian regression fitting algorithm. The fitted profiles are then shifted according to a two-point model to determine the LCFS.

For both views, the ELM synchronized profiles in figures 3(*b*)–(*e*) for ionization and neutral density are highest 3 ms after the ELM. The neutral density stays elevated for a few milliseconds before decreasing to an approximately constant profile and is closely tied to the evolution of the steepest density gradient in the pedestal. The ionization rate decreases to a steady-state in approximately 10 ms. Neutral density and ionization behavior is qualitatively similar on the LFS to that in [38] on AUG. However, on AUG the neutral density and ionization rate decrease on closed field lines for the first few milliseconds after the ELM which is unobserved on DIII-D.

Notable asymmetries exist between the two LLAMA views, highlighting the poloidal nature of the ionization source. While our source investigation cannot perform a full poloidal accounting of the ionization and neutral density behavior, LLAMA measurements provide local poloidal behavior at two locations. In general, edge fueling is suspected, both from experiment and modeling, to be poloidally dependent, and further complicated by poloidally asymmetric divertor conditions [39–41]. In this discharge, there is an order of magnitude asymmetry in the peak ionization rate which has recently been captured with XGC modeling [42]. The HFS ionization peak is pushed farther out onto the open field lines, consistent with density asymmetries which have been inferred

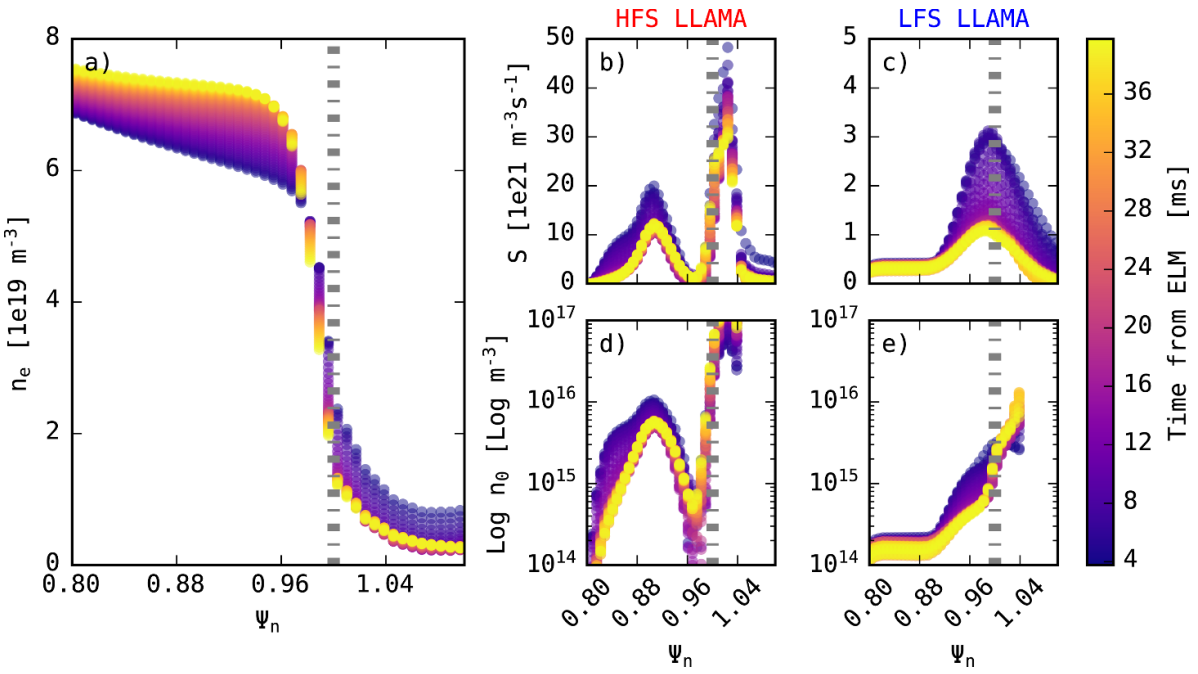

Figure 3. Time evolution of the electron density (*a*), deuterium ionization rate (*b*) and (*c*), and deuterium neutral density profiles (*d*) and (*e*) after an ELM. Profiles are the result of the average evolution over multiple ELM cycles in absolute time from the onset of the previous ELM.

on open and closed field lines during EDA H-mode in Alcator C-Mod [43], tied to SOL flows on open field lines in C-Mod [44], on open field lines in L-mode on AUG [45] and C-Mod [46], near the divertor on DIII-D [47], and above the active divertor on AUG [48] Furthermore, on the HFS, a second peak in brightness is observed around Ψ_N of 0.93. This results in an inferred peak in ionization and neutral density, shown in figures 3(*b*)–(*d*), where the electron temperature would suggest deuterium would have already ionized. It is an ongoing effort to investigate the underlying mechanism that causes this feature, which is commonly seen in many LSN discharges and tracks with plasma movement.

5. Inferred main ion perturbed transport coefficients

Source measurements during the rebuild period of the density profile after the ELM crash offer a unique opportunity to explore transport in the pedestal region. ELM's are an edge phenomenon which do not require external perturbation. The dynamic evolution of the electron density and temperature profiles allows investigation of the individual transport coefficients. With direct quantitative experimental profiles of the ionization source in the pedestal, transport coefficient evaluation can be performed on the ELM cycle with decreased uncertainty and without appealing to additional edge modeling. Multiple methods, including flux-gradient linear fitting and more advanced Bayesian inference inside the ImpRad OMFIT module, which utilizes the Aurora forward model, are employed [49, 50]. While time independent transport coefficients can describe the experimental data within error bars, temperature profile evolution and fits of the density profile suggest that the transport coefficients are actually time dependent. Aurora facilitates modeling of time-dependent transport, which is difficult to capture with the flux-gradient method. Importantly, with either method of analysis, time-dependent or time-independent, the inferred transport coefficients are consistent with an inward pinch on the order of $1\,\mathrm{m\,s^{-1}}$ inside of $\Psi_N \sim 0.99$.

For experimental investigation of the v and D coefficients inside the LCFS, transport is assumed to be purely radial which for the the continuity equation yields:

$$\frac{\partial n}{\partial t} = -\frac{1}{r}\frac{\partial}{\partial r}(r\Gamma) + S \tag{3}$$

and the linear flux gradient relation:

$$\Gamma = -D\frac{\partial n}{\partial r} + vn. \tag{4}$$

The radial coordinate r is a plasma volume (V) weighted by mapping the 2D flux surface volumes to a 1D cylindrical geometry, and is given by:

$$r = \sqrt{\frac{V}{2\pi^2 R_{\mathbf{axis}}}} \tag{5}$$

where $R_{\mathbf{axis}}$ is the magnetic axis. Notably, equation (4) assumes that the flux is linearly related to the gradients and absolute values of the density, which may be insufficient for large changes in gradient. Furthermore, the assumption of purely radial transport and linear flux relationship is likely insufficient in the scrape off layer (SOL) [51]. Even in the pedestal region, purely radial transport is a significant simplification as the asymmetries in the source shown in figures 3(*b*) and (*c*) and predicted in 2D modeling on DIII-D emphasize

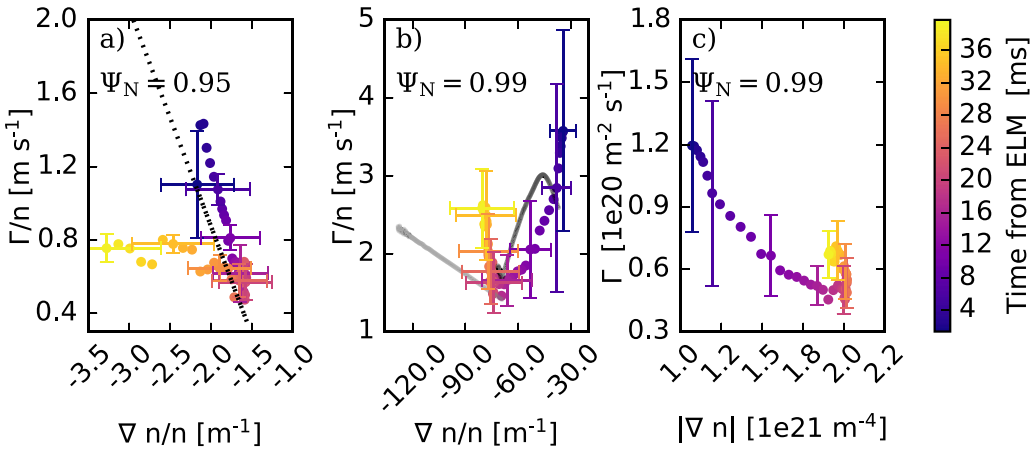

Figure 4. Flux gradient evolution during the density pedestal rebuild after an ELM at the top of the pedestal (*a*). At the pedestal top a D and v coefficient of $1\,\mathrm{m^2\,s^{-1}}$ and $-1\,\mathrm{m\,s^{-1}}$ respectively are found. (*b*) Near the LCFS, the flux-gradient evolution implies a non-physical negative D coefficient. The black line highlights the IMPRAD minimization result which captures the positive slope behavior with time dependent transport near the LCFS. The grey line shows the IMPRAD minimization with time-independent transport, which cannot recreate a positive slope, (*c*) the un-normalized flux-density behavior near the LCFS shows behavior consistent with a saturated gradient around $2\times10^{21}\,\mathrm{m^{-4}}$ after 20 ms.

the importance of poloidal flows [4, 52, 53]. However, the experimental approach detailed here should agree with the flux surface averaged result of 2D codes. Also, purely radial transport which captures both D and v is the most detailed experimental examination to date.

With the addition of the LLAMA measurements, the flux in equation (3) becomes experimentally constrained:

$$\Gamma(r,t) = \frac{1}{r}\int_0^r \left(S(r',t) - \frac{\partial n(r',t)}{\partial t}\right) r'dr' \qquad (6)$$

where the temporal and radial dependencies of variables are explicitly noted. The time rate of change of the density profile is obtained from the 2D fitting of electron density measurements in temporal and spatial domain, scaled by the carbon measurements as discussed in section 2. The source is determined by LLAMA. The LFS LLAMA system is utilized for the particle source. A flux surface average of the two views is avoided since greater insight into the poloidal source distribution would be required. Moreover, the HFS lacks diagnostic measurement of the density which likely accompany the source asymmetry observed by LLAMA. The main ion particle source from the neutral beam heating system, typically an order of magnitude smaller than the LLAMA source, is included in the S term by modeling of the time independent particle beam deposition profile using NUBEAM [54].

A simple method of investigating the transport coefficients is to divide equation (4) by n, recasting the equation in a linear form with the D coefficient as the slope and the v as the y-intercept. Since the D coefficient can only be positive, a negative slope is expected, giving a positive D coefficient. Figures 4(*a*) and (*b*) shows the result of applying this analysis at two locations in the pedestal, Ψ_N of 0.95 and 0.99 respectively. At Ψ_N of 0.95, the data is fit in a least squares fashion shown in the dotted black line. A negative slope is observed resulting in an inferred particle pinch of $1\pm1\,\mathrm{m\,s^{-1}}$ and diffusion coefficient of $1.0\pm0.7\,\mathrm{m^2\,s^{-1}}$. The dominant error comes from the density fitting algorithm's temporal and radial smoothing parameters. While two branches are apparent in figure 4(*a*), only one line is fit to the data, including the time range from 3 to 40 ms. The apparent separation of the two branches is dependant on the temporal smoothing parameter chosen in the 2D gaussian density fitting algorithm. While the separate branches could suggest distinct periods of transport, the separation of the branches can be reduced to agreement within errorbars with changes in temporal smoothing.

At Ψ_N of 0.99, a clear period of positive slope is observed after the ELM. If a fit were applied at Ψ_N of 0.99, as done at Ψ_N of 0.95, it would imply a non-physical negative D coefficient. Since the diffusion coefficient is strictly positive, the time-independent transport coefficient with the purely radial diffusive-convective ansatz is insufficient to describe the data near the LCFS. To explore the possible limits of our ansatz, figure 4(*c*) re-plots the data in figure 4(*b*) as a comparison of the flux versus pedestal gradient. The flux gradient evolution is suggestive of saturated gradient behavior. As seen in figure 3(*c*), early on in the rebuild there is an elevated edge source. As the density gradient steepens, it eventually reaches a fixed value, after which the flux evolves without changing density gradient. However, both the positive slope in figure 4(*b*) and distinct branches of linear behavior in figure 4(*a*) are suggestive of time-dependent transport coefficients.

The time-dependent transport coefficient idea is further supported by the evolution of η_e. η_e is defined as:

$$\eta_e = \frac{\lambda_{n_e}}{\lambda_{T_e}} \qquad (7)$$

where λ_x is the gradient length scale given by:

$$\lambda_x = \frac{x}{\nabla x}. \qquad (8)$$

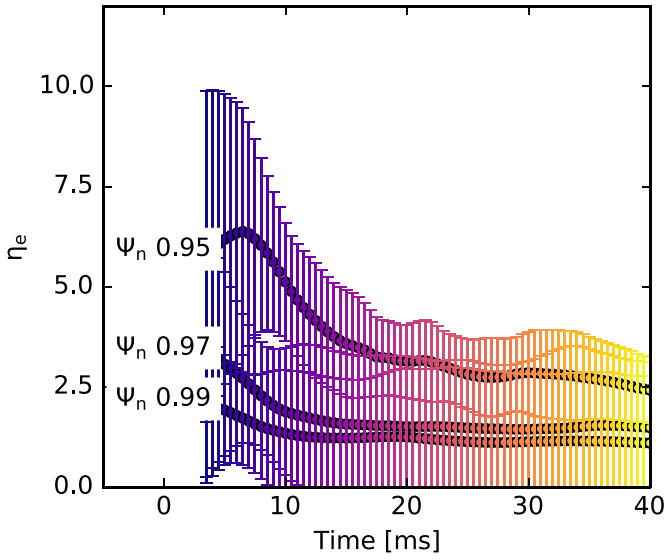

Figure 5. Evolution of η_e at three radial locations in the pedestal. η_e evolves for ∼18 ms.

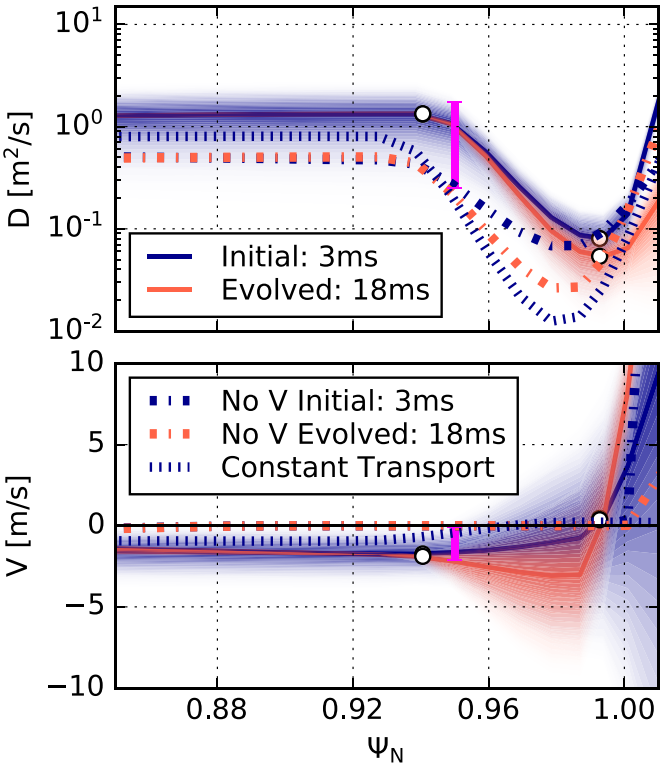

Figure 6. Density transport coefficient profiles of deuterium from the IMPRAD minimization routine of the ELM evolution. The minimization with no restrictions on the pinch is shown in solid lines with time-dependent transport for the outer two knots. The spline knots are shown in black outlined circles. Results from IMPRAD minimization with time independent transport and a forced convection of 0 m s^{-1} in the pedestal are shown in the dotted and dash dotted lines respectively. The Magenta points highlight the result from figure 4(*a*).

In experiment and simulation, η_e has been linked to transport in the pedestal [55–57]. In figure 5, the evolution of η_e is highlighted for three radial locations in the pedestal. η_e saturates around 18 ms after the ELM at values of ∼3 at Ψ_N of 0.95 and ∼1.5 at Ψ_N of 0.97 and 0.99. While these simple methods are illustrative of behavior in the pedestal, they are limited in conclusions due to the inability to capture the complex behavior near the LCFS and lack of constraint on continuity in the inferred D and v profiles.

To include the time-dependent transport coefficients, as well as radial continuity on the D and v profiles, forward modeling of the main ion and inference through the IMPRAD framework is performed using the Aurora package. Aurora, originally developed for impurity transport studies, was expanded by including as input the temporal and spatial experimental measurements from LLAMA of the main ion source to model main ion radial transport [58]. Aurora is a 1.5 dimensional model which couples the continuity equation to the v and D model described in equations (3) and (4) [50]. Similar to the flux-gradient approach for linear fitting, Aurora assumes that behavior can be captured by the purely radial diffusive-convective ansatz using the radial coordinate in equation (5) inside the LCFS. Aurora does not constrain the evolution of impurity or main ion density profiles by quasi-neutrality. Bayesian inference is run inside IMPRAD, which iteratively runs Aurora varying the D and v profiles using a non-linear optimization method, LMFIT [59]. The minimization is run comparing the results of synthetic diagnostics of the forward model to the raw experimental density measurements. Time-dependent cases are included by specifying the beginning and end of the transport coefficient evolution. Transport is linearly evolved in time within that time period.

As inputs to the Aurora model, the initial main ion density 3 ms after the ELM is provided by the scaled fit to the electron density shown in figure 3(*a*). The LFS LLAMA source data and NUBEAM model of the NBI beam deposition of the profile are included as the main ion particle sources. The magnetic geometry from EFIT, and the beginning and end of transport coefficient evolution are also included as inputs. Transport is allowed to evolve from the beginning of the data analysis window, 3 ms, to the saturation period suggested by the evolution of η_e at approximately 18 ms. A summary of the Bayesian minimization parameters are shown in table 1. The minimization is run with five radial spline knots for both the v and D coefficients. The spline knot location is included in the minimization along with the values of the transport coefficients at those spline knots. A scaling of the LFS LLAMA source by a constant factor is included in the minimization to account for the uncharacterized poloidal variation of the source, shown as S in table 1. Furthermore, due to the time evolution suggested by the η_e evolution and positive slope in figure 4(*b*), the value of the transport coefficients for the two knots closest to the LCFS are allowed to vary in time.

Figure 6 shows the result of the minimization using the Aurora forward model for the time-dependent transport coefficients in the solid lines. The probability distribution for solutions are shown by the shaded regions surrounding the solid lines and are calculated from covariance matrix. Chi-square

Table 1. Table of the number of free parameters (NFP), mean of the distribution, and range or sigma of the distribution for Bayesian inference in IMPRAD. For the range or sigma column, if a single number is listed, it represents the standard deviation of a Gaussian distribution.

Quantity	NFP	Mean					Range or Sigma				
D at 3 ms ($m^2\,s^{-1}$)	7	0.2	0.3	1.3	0.06	5	All variables 0.01–100				
D at 18 ms ($m^2\,s^{-1}$)					0.04	0.04					
D knot location (ρ_p)	5	0.2	0.5	0.97	1.0	1.2	0–1.1				
v at 3 ms ($m\,s^{-1}$)	7	0	0.1	−2	−1	20	2.5	2.5	50	100	100
v at 18 ms ($m\,s^{-1}$)					−4	28				100	100
v knot location (ρ_p)	5	0.2	0.5	0.97	1.0	1.2	0–1.1				
S scale	1	1					1.6				

per degree of freedom for the minimization is 1.4. The blue line shows the transport coefficients at 3 ms and the orange color is for 18 ms. The transport linearly varies from the blue profile to the orange profile within that time period. For the remaining analyzed period of the ELM cycle, up to 40 ms, the transport coefficients are fixed at the orange profile. The diffusion and convection coefficients at Ψ_N of 0.95 from figure 4(*a*) are shown in magenta. The resulting normalized flux gradient trajectory is shown in black in figure 4(*b*). The time-dependent transport evolution can recreate the positive slope behavior observed in the simplistic flux gradient method.

Throughout the transport coefficient evolution an inward pinch exists in the steep density gradient region of the pedestal. Near the LCFS, and on open field lines, the convection becomes radially outward and grows to a maximum value of approximately 30 $m\,s^{-1}$, broadly consistent with previous estimates of the near SOL effective radial convection on DIII-D in L-mode of 10 to 30 $m\,s^{-1}$ and far SOL estimates in both H-mode and L-mode of ∼100 $m\,s^{-1}$ [60, 61]. Magnitudes of the convection and diffusion coefficients in the pedestal are similar in magnitude with previous experimental investigations which utilized modeled edge ionization sources [5, 20, 21]. In particular, on DIII-D, an inward pinch has been suggested, though not estimated, and an estimate for a purely diffusive transport found a minimum of 0.03 $m^2\,s^{-1}$ in the pedestal in comparison to the 0.05 $m^2\,s^{-1}$ found here [5, 23]. The minimization scales the source by a factor of 1.2, suggesting that the LFS LLAMA slightly under predicts the flux-surface average particle flux. The scaling factor is at least qualitatively inline with 2D modeling of LSN DIII-D discharges, which show reduced source above the midplane relative to below the midplane but asymmetry between the HFS and LFS below the midplane [4, 52].

To examine if purely diffusive transport in the pedestal or constant transport can describe the experimental data, two additional minimizations are run. One minimization, labeled constant transport, enforces time independent transport coefficients for all knots. The other forces $v = 0$ (no convection) at Ψ_N of 0.93 and Ψ_N of 0.99, the two knots in the pedestal region found to have a pinch in the unrestricted time-dependent case. The no convection minimization still allows the same time-dependent transport evolution for the outer two knots of diffusion and the outermost knot of convection. Figure 6 shows the result of the minimization for the time independent and no convection scenarios, in dotted and dash dotted lines respectively. Due to the high scatter in the TS measurements, the synthetic diagnostic results for both of these minimizations capture the density trajectory within error bars, with comparable chi-square per degree of freedom of 1.5. The time independent transport coefficients still show an inward pinch in the pedestal, although with smaller magnitude. However, the time-independent transport coefficients, are not able to recreate the positive slope behavior observed at Ψ_N of 0.99 in the first ∼20 ms in the density rebuild. This is shown by the IMPRAD trajectory for the time-independent case by the grey line in figure 4(*b*). While the time-dependent no pinch scenario can recreate the positive slope behavior, it predicts large radial fluxes of approximately 300 $m\,s^{-1}$ in the near scrape of layer (not shown). Furthermore, both the constant transport and time-dependent transport predict diffusion coefficients on the order of 0.5 $m\,s^{-2}$ throughout the core of the plasma. The low-core diffusion disagrees with previous studies of D on DIII-D, which found maximum D coefficients in the core of at least 1 $m^2\,s^{-1}$ [11, 12]. Similarly, methods have estimated peak core D on other machines in the 1–10 $m^2\,s^{-1}$ range [22, 62].

6. Discussion and conclusion

The density pedestal rebuild after an ELM crash is utilized to examine the contributions of diffusion and convection in forming the density pedestal on DIII-D. Absolutely calibrated time-dependent edge ionization and neutral density measurements are obtained from the LLAMA diagnostic, allowing experimental calculation of the ionization source terms in the continuity equation. Density fit profiles and evolution of η_e in the pedestal are suggestive of time-dependent transport coefficient evolution in the pedestal during the inter-ELM period. IMPRAD and the Aurora transport code have been extended to model main ion transport coefficients, including time-dependent transport. The fast computation speed of Aurora is exploited to run minimization algorithms with time-dependent transport coefficients and the results are consistent with an inward particle pinch of a few meters per second. Optimization

of time independent transport coefficients further supports the presence of an inward particle pinch in the steep density gradient. While the case of no convection in the pedestal cannot be ruled out, modeling suggests the phenomenon would need to be accompanied by diffusion in the core of the tokamak which is lower than that found in previous studies, along with the need for large convection in the near SOL.

While the time-dependent transport coefficients and source dynamics presented here offer an advance over previous attempts to measure main ion particle transport in the pedestal, fundamental uncertainties remain. Aurora and IMPRAD facilitate modelling of time-dependent transport evolution, but the period of evolution and temporal form of the evolution are specified as inputs, and not included in the minimization routines. While the time-dependent results shown here are generally robust to alterations in the specified period of transport coefficient evolution, the error bars do not include these uncertainties. Furthermore, the full poloidal distribution of the hydrogen ionization source is not fully constrained by experimental LLAMA measurements, and the dynamics observed on the HFS and LFS show significant poloidal asymmetries. Finally, the possibly time-dependent effects of the impurity ions and the divertor neutral source have been excluded from this analysis.

Future analysis should attempt to investigate scenarios which reduce these uncertainties: increasing the poloidal coverage for measurements of the ionization source, reducing or better constraining the contributions of impurity ions, and operating in plasmas without neutral beam heating. Experimental source measurements and the IMPRAD framework developed for this work offer opportunities to analyze an increasing number of discharges to further investigate the role and scalings of diffusion and convection in the density pedestal.

Acknowledgments

This material is based upon work supported by the U.S. Department of Energy, Office of Science, Office of Fusion Energy Sciences, using the DIII-D National Fusion Facility, a DOE Office of Science user facility, under Awards DE-SC0014264, DE-AC02-09CH11466, and DE-FC02-04ER54698.

Disclaimer

This report was prepared as an account of work sponsored by an agency of the United States Government. Neither the United States Government nor any agency thereof, nor any of their employees, makes any warranty, express or implied, or assumes any legal liability or responsibility for the accuracy, completeness, or usefulness of any information, apparatus, product, or process disclosed, or represents that its use would not infringe privately owned rights. Reference herein to any specific commercial product, process, or service by trade name, trademark, manufacturer, or otherwise does not necessarily constitute or imply its endorsement, recommendation, or favoring by the United States Government or any agency thereof. The views and opinions of authors expressed herein do not necessarily state or reflect those of the United States Government or any agency thereof.

ORCID iDs

A.M. Rosenthal https://orcid.org/0000-0002-6149-1136
J.W. Hughes https://orcid.org/0000-0003-4802-4944
F.M. Laggner https://orcid.org/0000-0003-1601-2973
T. Odstrčil https://orcid.org/0000-0003-4173-4230
T.M. Wilks https://orcid.org/0000-0002-9675-678X
F. Sciortino https://orcid.org/0000-0002-5159-1889

References

[1] Jassby D.L. 1975 *Nucl. Fusion* **15** 453
[2] Groebner R.J., Mahdavi M.A., Leonard A.W., Osborne T.H., Porter G.D., Colchin R.J. and Owen L.W. 2002 *Phys. Plasmas* **9** 2134–40
[3] Fenstermacher M.E. *et al* (The DIII-D Team) 2005 *Nucl. Fusion* **45** 1493–502
[4] Sontag A.C., Chen X., Canik J., Leonard A., Lore J.D., Moser A.L., Murakami M., Park J.M. and Petty C. 2017 *Nucl. Fusion* **57** 076025
[5] Callen J., Groebner R., Osborne T., Canik J., Owen L., Pankin A., Rafiq T., Rognlien T. and Stacey W. 2010 *Nucl. Fusion* **50** 064004
[6] Wolfrum E. *et al* 2017 *Nucl. Mater. Energy* **12** 18–27
[7] Mahdavi M.A. *et al* 2002 *Nucl. Fusion* **42** 52
[8] Rosenthal A.M. *et al* 2021 *Rev. Sci. Instrum.* **92** 033523
[9] Laggner F.M., Bortolon A., Rosenthal A.M., Wilks T.M., Hughes J.W., Freeman C., Golfinopoulos T., Nagy A., Mauzey D. and Shafer M.W. (The DIII-D Team) 2021 *Rev. Sci. Instrum.* **92** 033522
[10] Mordijck S. 2020 *Nucl. Fusion* **60** 082006
[11] Mordijck S. *et al* 2020 *Nucl. Fusion* **60** 066019
[12] Mordijck S. *et al* 2015 *Nucl. Fusion* **55** 113025
[13] Tanaka K., Kawahata K., Tokuzawa T., Okajima S., Ito Y., Muraoka K., Sakamoto R., Watanabe K., Morisaki T. and Yamada H. (The LHD Experimental Group) 2008 *Plasma Fusion Res.* **3** 050
[14] Takenaga H., Nagashima K., Sakasai A., Oikawa T. and Fujita T. 1998 *Plasma Phys. Control. Fusion* **40** 183–90
[15] Tanaka K. *et al* (LHD Experimental Group) 2005 *Nucl. Fusion* **46** 110
[16] Gentle K.W., Richards B. and Waelbroeck F. 1987 *Plasma Phys. Control. Fusion* **29** 1077
[17] Hughes J.W., LaBombard B., Terry J., Hubbard A. and Lipschultz B. 2007 *Nucl. Fusion* **47** 1057–63
[18] LaBombard B. *et al* (Alcator C-Mod Team) 2008 *Phys. Plasmas* **15** 056106
[19] Schuster C.U., Wolfrum E., Fable E., Fischer R., Griener M., Tal B., Angioni C., Eich T., Manz P. and Stroth U. (The ASDEX Upgrade Team) 2022 *Nucl. Fusion* **62** 066035
[20] Willensdorfer M., Fable E., Wolfrum E., Aho-Mantila L., Aumayr F., Fischer R., Reimold F., Ryter F. and (The ASDEX Upgrade Team) 2013 *Nucl. Fusion* **53** 093020
[21] Ohtani Y., Yoshida M., Honda M. and Narita E. 2021 *AIP Adv.* **11** 085306
[22] Ohtani Y., Tanaka K., Tokuzawa T., Akiyama T., Yamada L., Yasuhara R., Funaba H., Shoji M. and Goto M. (LHD Experimental Group) 2020 *Plasma Phys. Control. Fusion* **62** 025029

[23] Leonard A.W., Elder J.D., Canik J.M., Groebner R.J. and Osborne T.H. 2013 *J. Nucl. Mater.* **438** S246–9
[24] Eldon D. *et al* 2012 *Rev. Sci. Instrum.* **83** 10E343
[25] Chrystal C., Burrell K.H., Grierson B.A., Haskey S.R., Groebner R.J., Kaplan D.H. and Briesemeister A. 2016 *Rev. Sci. Instrum.* **87** 11E512
[26] Chilenski M.A., Greenwald M.J., Hubbard A.E., Hughes J.W., Lee J.P., Marzouk Y.M., Rice J.E. and White A.E. 2017 *Nucl. Fusion* **57** 126013
[27] Lehecka T., Peebles W.A., Luhmann N.C. and Carlstrom T.N. 1988 *Rev. Sci. Instrum.* **59** 1580–1
[28] Odstrčil T., Pütterich T., Odstrčil M., Gude A., Igochine V. and Stroth U. (ASDEX Upgrade Team) 2016 *Rev. Sci. Instrum.* **87** 123505
[29] Summers H.P., Dickson W.J., O'Mullane M.G., Badnell N.R., Whiteford A.D., Brooks D.H., Lang J., Loch S.D. and Griffin D.C. 2006 *Plasma Phys. Control. Fusion* **48** 263–93
[30] Odstrcil T., Laggner F.M., Rosenthal A.M., Bortolon A., Hughes J.W., Spendlove J.C. and Wilks T.M. 2022 *Rev. Sci. Instrum.* **93** 103503
[31] Stangeby P.C., Canik J.M., Elder J.D., Lasnier C.J., Leonard A.W., Eldon D., Makowski M.A., Osborne T.H. and Grierson B.A. 2015 *Nucl. Fusion* **55** 093014
[32] Connor J.W. 1998 *Plasma Phys. Control. Fusion* **40** 531
[33] Banerjee S., Mordijck S., Barada K., Zeng L., Groebner R., Osborne T., Rhodes T.L., Snyder P.B., Grierson B. and Diallo A. 2021 *Nucl. Fusion* **61** 056008
[34] Diallo A., Groebner R.J., Rhodes T.L., Battaglia D.J., Smith D.R., Osborne T.H., Canik J.M., Guttenfelder W. and Snyder P.B. 2015 *Phys. Plasmas* **22** 056111
[35] Burckhart A., Wolfrum E., Fischer R., Lackner K. and Zohm H. 2010 *Plasma Phys. Control. Fusion* **52** 105010
[36] Laggner F.M., Diallo A., Cavedon M. and Kolemen E. 2019 *Nucl. Mater. Energy* **19** 479–86
[37] Diallo A. and Laggner F.M. 2020 *Plasma Phys. Control. Fusion* **63** 013001
[38] Bogar K., Geiger B., Schneider P., Jansen van Vuuren A. and Grover O. (The ASDEX Upgrade Team and The EUROfusion MST1 Team) 2021 *Nucl. Fusion* **61** 036001
[39] Groth M. *et al* (The DIII-D and ASDEX Upgrade Teams and JET EFDA Contributors) 2011 *Plasma Phys. Control. Fusion* **53** 124017
[40] Hollmann E.M., Brezinsek S., Brooks N.H., Groth M., McLean A.G., Pigarov A.Y. and Rudakov D.L. 2006 *Plasma Phys. Control. Fusion* **48** 1165–80
[41] Pshenov A.A., Kukushkin A.S. and Krasheninnikov S.I. 2017 *Phys. Plasmas* **24** 072508
[42] Wilkie G.J., Laggner F.M., Hoe K.S., Hager R., Churchill M., Bortolon A. and Chang C. 2022 Kinetic simulation of DIII-D pedestal fueling asymmetry with synthetic diagnostics *64th Annual Meeting of the APS Division of Plasma Physics (Bulletin of the American Physical Society)* (*Spokane, Washington, United States of America*, *17–21 October 2022*) (American Physical Society) (available at: http://meetings.aps.org/Meeting/DPP22/Session/PO05.14)
[43] Churchill R.M. *et al* (Alcator C-Mod Team) 2015 *Phys. Plasmas* **22** 056104
[44] LaBombard B. *et al* (The Alcator Group) 2004 *Nucl. Fusion* **44** 1047
[45] Hachmeister D., Silva C., Santos J., Conway G., Gil L., Silva A., Stroth U., Vicente J. and Wolfrum E. 2022 *J. Instrum.* **17** C01008
[46] LaBombard B. *et al* 2017 *Nucl. Mater. Energy* **12** 139–47
[47] Carlstrom T.N., Glass F., Du D., McLean A.G., Taussig D. and Boivin R. 2018 *Rev. Sci. Instrum.* **89** 10C111
[48] Potzel S. *et al* 2015 *J. Nucl. Mater.* **463** 541–5
[49] Takenaga H. *et al* 1995 *Nucl. Fusion* **35** 107
[50] Sciortino F. *et al* 2021 *Plasma Phys. Control. Fusion* **63** 112001
[51] Naulin V. 2007 *J. Nucl. Mater.* **363–365** 24–31
[52] Groth M. *et al* 2019 *Nucl. Mater. Energy* **19** 211–7
[53] Sang C., Guo H., Stangeby P., Wang H., Wang L. and Wang D. 2020 *Nucl. Fusion* **60** 056011
[54] Pankin A., McCune D., Andre R., Bateman G. and Kritz A. 2004 *Comput. Phys. Commun.* **159** 157–84
[55] Hatch D.R. *et al* (JET Contributors) 2019 *Nucl. Fusion* **59** 086056
[56] Chapman-Oplopoiou B. *et al* 2022 *Nucl. Fusion* **62** 086028
[57] Guttenfelder W., Groebner R.J., Canik J.M., Grierson B.A., Belli E.A. and Candy J. 2021 *Nucl. Fusion* **61** 056005
[58] Sciortino F. *et al* 2022 *Plasma Phys. Control. Fusion* **64** 124002
[59] Newville M., Stensitzki T., Allen D.B. and Ingargiola A. 2014 LMFIT: non-linear least-square minimization and curve-fitting for Python (available at: https://zenodo.org/record/11813)
[60] Lipschultz B., Whyte D. and LaBombard B. 2005 *Plasma Phys. Control. Fusion* **47** 1559–78
[61] Whyte D.G., Lipschultz B.L., Stangeby P.C., Boedo J., Rudakov D.L., Watkins J.G. and West W.P. 2005 *Plasma Phys. Control. Fusion* **47** 1579
[62] Maslov M. *et al* (JET Contributors) 2018 *Nucl. Fusion* **58** 076022